A Comparison of Observed and Numerically Simulated Circulation in the Cayman Sea

ROBERT L. MOLINARI

Atlantic Oceanographic and Meteorological Laboratories, NOAA, Miami, Fla. 33149

(Manuscript received 24 October 1973, in revised form 12 May 1974)

ABSTRACT

An observational and numerical study of the circulation in the Cayman Sea is presented. Data taken in three different years suggest a common February to May circulation pattern. A well-developed current crosses 85W south of the Cayman Ridge. An anticyclonic eddy in the central basin appears to be a common feature of this season's circulation. Finally, the data from these cruises consistently portray significant accelerations occurring in the vicinity of Cozumel Island where the flow merges with the Yucatan Current. A different pattern is inferred from data collected in July and August. The north component of the flow over the western edge of the Cayman Ridge appears to determine the type of flow regime observed.

The numerical model is based upon predictive equations for the vorticities in a two-layer ocean on a beta-plane, and includes topographic, advective and friction effects. The model is driven by lateral input boundary conditions derived from an April–May 1968 observational study. The baroclinic western boundary current of the numerical model develops in response to eastern input boundary conditions, while the barotropic current is constrained to intensify and flow along the continental slopes.

1. Introduction

The western Caribbean Sea Basin is shown schematically in Fig. 1. Historically, this area also has been called the Cayman Sea, although it is comprised of both the Cayman Basin and the Yucatan Basin. In the present study, the term Cayman Sea will be used to denote the western Caribbean Sea, just north of Honduras and west of 83W longitude.

Cochrane (1971) has discussed the April–May circulation of the Cayman Sea and the Yucatan Strait. The data consistently portray a flow regime dominated by an anticyclonic loop in the central basin, and a strong Yucatan Current on the western boundary. Cochrane considers bottom topography to be an important factor in determining the flow pattern.

The Yucatan Current has been described as a western boundary current similar in dynamics to the Gulf Stream (Cochrane, 1969). Saylor (1963), applying a variation of the Charney-Morgan inertial model, concluded that the conservation of potential vorticity could explain the formation of the Yucatan Current. However, Ahrens (1965), in an analysis of available hydrographic data, found that potential vorticity was not conserved along the Current and attributed the gain of cyclonic vorticity to frictional effects.

A marked association between the highest surface velocities of the Yucatan Current and a relatively constant depth has been noted in the vicinity of the Yucatan Channel by Cochrane (1966). Molinari and Cochrane (1972), assuming the conservation of potential vorticity and using observed data for initial conditions, calculated paths of the current core which were similar to observed paths from the Yucatan Strait to 23°30′N. At 23°30′N the Current separates from the Campeche Bank and enters the Gulf of Mexico Basin.

The present investigation is an attempt to study the circulation patterns of the Cayman Basin, and the dynamics of the formation of the Yucatan Current. In particular, the western boundary character of and the effect of topography upon the flow are considered. Observations available from various cruises in the area are analyzed to identify important features of the Cayman Sea current pattern. Finally, a predictive numerical model of the circulation is used in an attempt to ascertain the important dynamical parameters affecting the flow.

2. Circulation deduced from available data

In order to specify the boundary conditions which will be required in the two-layer numerical model, and to describe the observed baroclinic flow, an Equivalent Baroclinic Height (EBH) parameter is introduced. The EBH is derived, as illustrated in Fig. 2, by equating the area under an observed σ_t-depth curve to the area under an equivalent two-layer σ_t-depth curve. The observed σ_t-depth area is calculated by numerically integrating from the surface to a level of small density gradients ($\sigma_t=27.75$). The EBH is then obtained by dividing this area by an average density difference ($\Delta\sigma_t=2.5\times10^{-3}$). Fofonoff (1962) qualitatively defines the baroclinic flow component in an analogous manner.

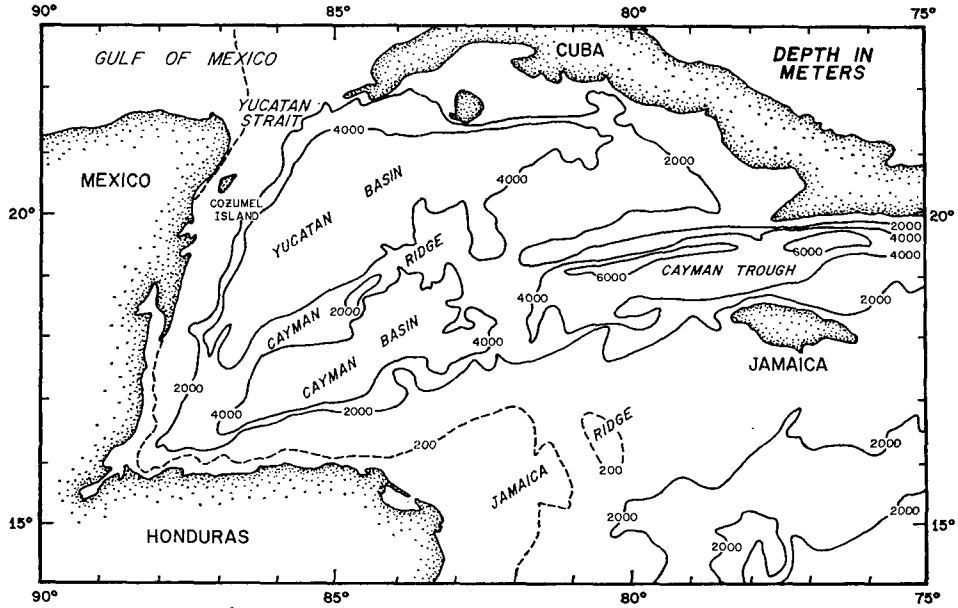

FIG. 1. The Cayman Sea (western Caribbean Sea), and its major topographic features.

The observational data taken during the spring of 1933, 1961 and 1968 all suggest a similar circulation pattern. March 1961 and April–May 1968 EBH data given in Figs. 3 and 4, respectively, show the dominant features of the flow.

During both years the major portion of the flow through the Yucatan Strait crossed 85W as an intense coherent current south of the Cayman Ridge. The current had a predominantly westerly drift at this longitude. In 1968, a closed eddy was centered at approximately 85°30′W, 19°30′N (Fig. 3). The 1961 data do not permit closure of the contours but they do indicate a similar circular pattern centered to the east of the 1968 feature (Fig. 4). During both years the western intensification convergence of the isopleths occurs at the vicinity of and north of Cozumel Island.

The April–May 1933 and February 1961 data, although sparse, present further evidence for a common spring circulation pattern. Since neither field can be contoured, only the EBH values and the direction of the EBH computed velocity are given for the February 1961 data on Fig. 3, and for the 1933 data on Fig. 4. The EBH values of the 1933 field closely correspond to those of the 1968 field, suggesting a similar inflow south of the Cayman Ridge and a similar position and intensity for the eddy. The February 1961 data depict a corresponding but shallower baroclinic field than given by the late March 1961 data.

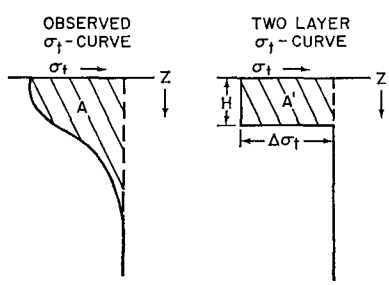

FIG. 2. Schematic diagram illustrating the Equivalent Baroclinic Height (EBH) parameter H.

The geostrophic volume transport per unit width per unit time of the baroclinic component is defined by the relation

$$T=\frac{g\epsilon}{2f}(H^2-H_0^2), \tag{1}$$

where g is the acceleration of gravity, ϵ the relative density anomaly (2.5×10^{-3}), f the Coriolis parameter, H the value of EBH, and H_0 the value of EBH contour at the coastal boundary. Longitudinal sections of transport are given in Fig. 5 and zonal sections in Fig. 6.

The longitudinal sections of Fig. 5a are very similar in that between 20 and 30×10^6 m^3 s^{-1} entered the basin south of the Cayman Ridge. The spike in the April–May 1933 data at 17°30′ (Fig. 5a) is apparently a function of the shallow depth at the station, and the flow regime it suggests is questionable. The March 1956 data shown in Fig. 5b represent the available information for this period, and possess the same property of intense flow south of the Cayman Ridge. Finally the March–April 1961 and May 1968 transport curves of Fig. 5c are further evidence for the similarity of circulation patterns during these periods.

Zonal cross sections of geostrophic transport for March–April 1961 and for May 1968 (Fig. 6) depict the western intensification process. The distances are

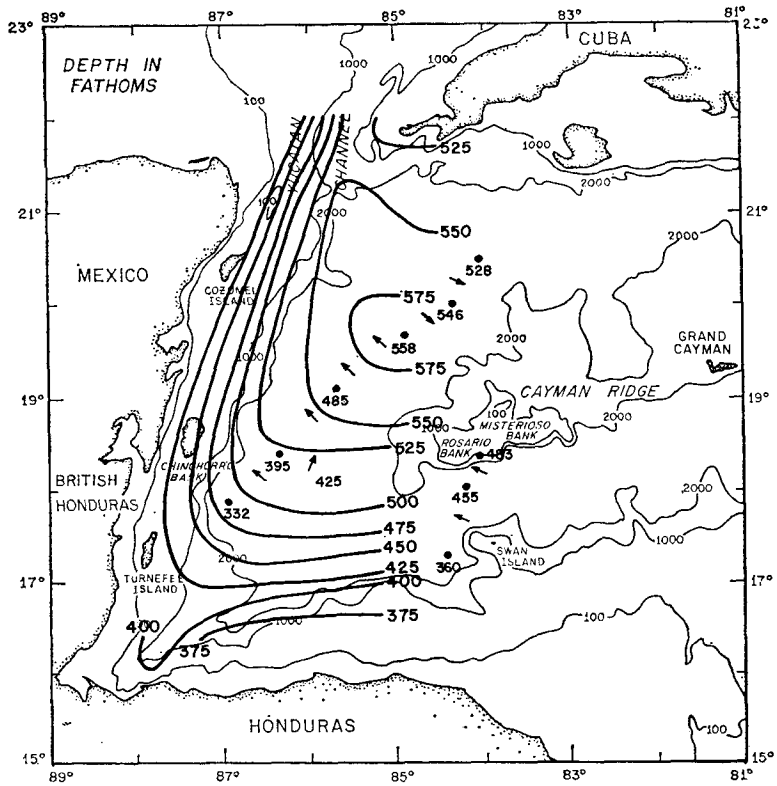

FIG. 3. Contours of EBH, in meters, determined from data taken in March 1961. Also shown are EBH values and directions of geostrophic flow computed from data collected in February 1961.

calculated from the H_0 contour. In both Figs. 6a and 6b the northerly flow is fully developed by 18°30′N. North of 18°30′N the increase in slope of the transport curves is a measure of western intensification. Both years have countercurrents indicated on the Cuban side of the Yucatan Strait.

A different circulation pattern can be inferred from data taken in August 1970 and July 1971. The data were expendable bathythermograph (XBT) profiles and thus EBH's could not be computed. Comparing the equivalent baroclinic heights with the corresponding T-z curves of various cruises indicates that, throughout the basin, the depth of the 11°C isotherm can be used as a first approximation of the EBH.

A map of the August 1970 11°C isothermal surface is given in Fig. 7, and the July 1971 surface in Fig. 8. July 1971 drifting buoy trajectories (Fig. 9) presented by Molinari and Starr (1972) suggest surface currents similar to those indicated by the temperature distribution of Fig. 8.

The major part of the 1970 current entering across the 85°30′W meridian is at a more northerly latitude than either the 1961 or 1968 currents (Figs. 3 and 4). In addition, the 1970 flow has a more northerly component at 85°30′W than indicated by the 1961 or 1968 data. Both the August 1970 and July 1971 figures (Figs. 7 and 8) suggest a considerable portion of the total flow through the Strait has joined the boundary current at more northerly latitudes than during the February to May cases.

3. The numerical model

a. Model formulation

The numerical model is essentially that of Wert and Reid (1972). The major assumptions and constraints of their formulation are that:

1) A two-layer ocean, each layer incompressible and with uniform density, is located on a beta-plane.
2) An influx of mass through an open boundary drives the upper layer, and an interlayer stress drives the lower layer.
3) All other driving forces, including wind and tidal effects are neglected.
4) Topography is allowed only in the lower layer.

Lateral and bottom friction as well as advection of momentum and of vorticity are allowed in the system.

In the following expressions, the east and north directions are represented by the x and y axes respectively Primed terms are lower layer variables, and unprimed terms are upper layer variables. The two-

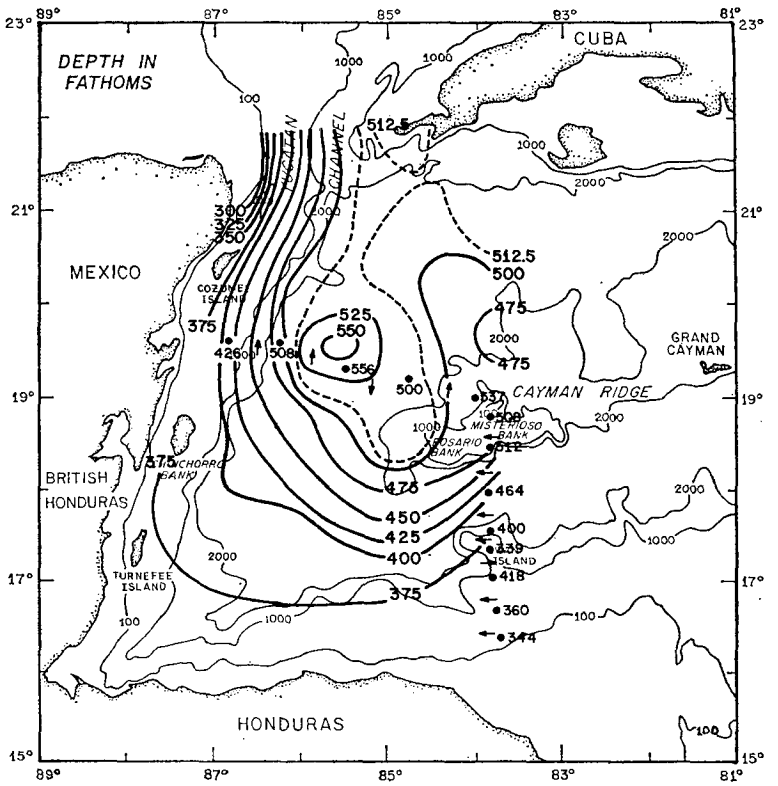

FIG. 4. Contours of EBH, in meters, determined from data taken in April–May 1968. Also shown are EBH values and directions of geostrophic flow computed from data collected in April–May 1933.

dimensional fluid velocity is represented by the vector $\mathbf{v}=u\mathbf{i}+v\mathbf{j}$. The H's are layer thicknesses, and D the undisturbed water depth. The frictional coefficients are lateral friction K, interlayer friction σ, and bottom friction σ'. With these symbols and the above assumptions, the vertically integrated equations of motion and the continuity equations can be written as

$$\frac{\partial \mathbf{v}}{\partial t}+(\mathbf{v}\cdot\nabla)\mathbf{v}+f\mathbf{k}\times\mathbf{v}+g\nabla(H+H'-D)$$

$$=-\sigma\left(\frac{\mathbf{v}-\mathbf{v}'}{H}\right)+K\nabla^2\mathbf{v}, \quad (2)$$

$$\frac{\partial \mathbf{v}'}{\partial t}+(\mathbf{v}'\cdot\nabla)\mathbf{v}'+f\mathbf{k}\times\mathbf{v}'+g\nabla\left(\frac{\rho}{\rho'}H+H'-D\right)$$

$$=\sigma\left(\frac{\mathbf{v}-\mathbf{v}'}{H'}\right)-\frac{\sigma'\mathbf{v}'}{H'}+K\nabla^2\mathbf{v}', \quad (3)$$

$$\frac{\partial H}{\partial t}+\nabla\cdot(H\mathbf{v})=0, \quad (4)$$

$$\frac{\partial H'}{\partial t}+\nabla\cdot(H'\mathbf{v}')+0. \quad (5)$$

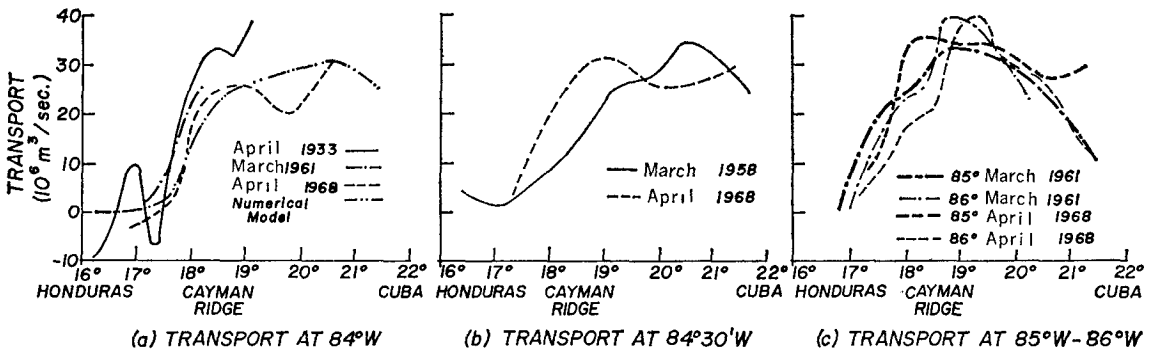

FIG. 5. Geostrophic baroclinic transports computed from Eq. (1) at 84W, 84°30'W and 85–86W. Panel (a) also includes the smoothed version of the April 1968 curve used to drive the numerical models.

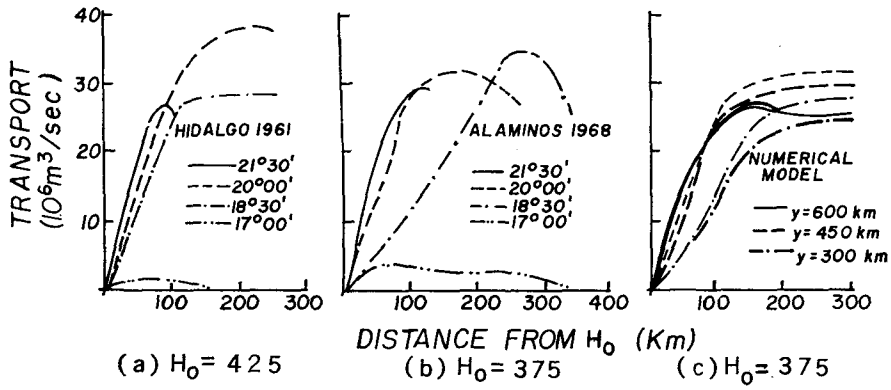

FIG. 6. Geostrophic baroclinic transports computed from Eq. (1) for March 1961, April–May 1968 and for the numerical model. The thicker lines of panel (c) were computed from the results of the non-topographic model, and the thinner lines from the topographic model.

A vorticity equation for each layer is formed from these equations. Prediction equations for H and H' are obtained from the vorticity equation by making the geostrophic approximation in each layer. The geostrophic constraint eliminates internal gravity waves. Moreover, the use of a rigid-lid condition on the sea surface ($H+H'-D$, independent of t) eliminates surface gravity waves.

The prediction equations for the baroclinic and barotropic modes, with

$$B\equiv\frac{\rho}{\rho'}H+H'-D, \tag{6}$$

$$\epsilon\equiv\frac{\rho'-\rho}{\rho'}, \tag{7}$$

are respectively

$$\epsilon\nabla^2\frac{\partial H}{\partial t}+\epsilon HJ\left[H,\frac{\zeta+f}{H}\right]+HJ\left[B,\frac{\zeta+f}{H}\right]$$
$$-H'J\left[B,\frac{\zeta'+f}{H'}\right]-\frac{f}{g}\frac{\partial H}{\partial t}\left[\frac{\zeta+f}{H}+\frac{\zeta'+f}{H'}\right]$$
$$=\frac{f}{g}\left[K\nabla^2(\zeta-\zeta')-\sigma(\zeta-\zeta')\left(\frac{1}{H}+\frac{1}{H'}\right)+\frac{\sigma'\zeta'}{H'}\right] \tag{8}$$

and

$$\nabla^2\frac{\partial B}{\partial t}+H'J\left[B,\frac{\zeta'+f}{H'}\right]+\frac{f}{g}\left(\frac{\zeta'+f}{H}\right)\frac{\partial H}{\partial t}$$
$$=\frac{f}{g}\left[\sigma\frac{(\zeta-\zeta')}{H'}-\frac{\sigma'\zeta'}{H'}+K\nabla^2\zeta'\right]. \tag{9}$$

The relative vortices are given by

$$\zeta=\zeta'+\frac{g\epsilon}{f}\nabla^2H \tag{10}$$

and

$$\zeta'=\frac{g}{f}\nabla^2B. \tag{11}$$

The Jacobians are used in the form

$$J(A,B)=\frac{\partial}{\partial y}\left(B\frac{\partial A}{\partial x}\right)-\frac{\partial}{\partial x}\left(A\frac{\partial A}{\partial y}\right), \tag{12}$$

for reasons discussed below.

The finite-difference analogues of Eqs. (8) and (9) were taken as those given by Wert and Reid (1972). In summary, centered difference forms are used for the time and space derivatives. The nonlinear instabilities caused by the advective terms are suppressed by the use of the form of the Jacobian given in Eq. (12) (Arakawa, 1966). The DuFort-Frankel scheme (Smith, 1965) was used to represent the lateral diffusion of vorticity because of its stable properties.

b. Boundary conditions

The basin used in the numerical model is shown schematically in Fig. 10. The model basin is rectangular with an east-west dimension of 300 km, and a north-south dimension of 600 km. The Yucatan Strait is modelled as 180 km wide.

Fig. 10 also gives the bottom topography of the model basin. The Cayman Ridge and its associated Banks are not modelled. To insure that the bottom topography is confined to the lower layer, the shallowest depth is 700 m. The continental slopes closely approximate those found in the Cayman Basin, and a Yucatan Channel sill depth of 1800 m in the model approximates the actual sill depth. In the lower left hand corner of Fig. 10 is given a portion of the space grid; the space increment $\Delta x=\Delta y=\Delta s=10$ km.

Mass inflow and outflow are allowed through the eastern boundary and the Yucatan Strait. Solid impermeable boundaries in the model basin exist along

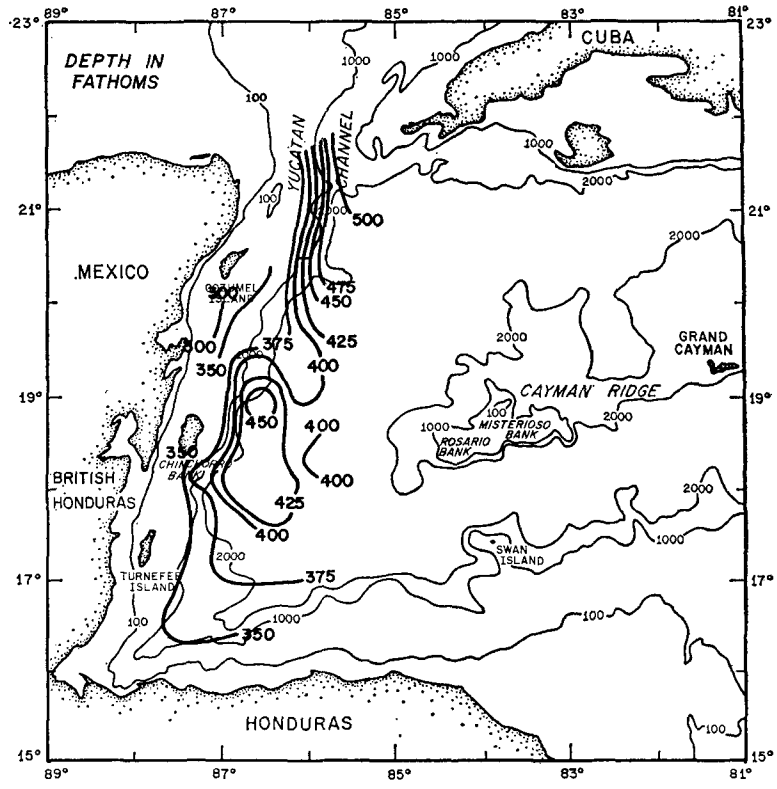

FIG. 7. The distribution of the depth, in meters, of the 11°C isotherm for August 1970.

the southern and western boundaries, and along that portion of the northern boundary to the east of the Yucatan Channel.

A schematic grid, shown in Fig. 11, will be used to demonstrate the boundary conditions applied to the various models. The inclusion of lateral friction requires two boundary conditions on all boundaries. To satisfy these conditions a fictitious boundary one space increment beyond the perimeter (the dots in Fig. 11) is introduced.

Two types of eastern boundary conditions are used to drive the interior baroclinic flow. In the first model this flow component is assumed normal to the open boundaries. If $x=i\Delta s$ and $y=j\Delta s$ on the numerical grid, then this boundary condition is given on the schematic grid as

$$H(7,j)=H(5,j).$$

Furthermore the values of $H(6,j)$ are given as an initial condition and held constant throughout the time integration. The following conditions are applied along the solid walls to satisfy the no-slip condition:

$$H(i,2)=H(2,j)$$
$$H(i,1)=H(i,3)$$
$$H(1,j)=H(3,j)$$
$$H(6,11)=H(5,11)\neq H(i,2)$$
$$H(i,12)=H(i,10).$$

Prediction of $H(2,11)$ and $H(3,11)$ at the Yucatan Strait requires the determination of $\zeta(2,12)$ and $\zeta(3,12)$. The method of Wert and Reid is followed in that ζ is determined from upstream conditions. For currents flowing out of the basin, ζ is determined by advecting potential vorticity; and for currents flowing into the basin, ζ is arbitrarily set outside the grid (Wert and Reid, 1972, p. 183).

A second model considers non-normal flow at the eastern forcing boundary. Again, $H(6,j)$ is both specified and constant with time. The assumption of non-normal flow requires that

$$H(7,j)=H(5,j)-\alpha(6,j)[H(6,j+1)-H(6,j-1)],$$

where

$$\alpha(6,j)=\tan^{-1}\left[\frac{v(6,j)}{u(6,j)}\right]$$

is given at $t=0$ and independent of time. The conditions along the solid boundaries and at the Yucatan Strait are identical to those of the preceeding model.

The barotropic flow parameter B is a predicted variable at both the eastern and Yucatan Channel openings. This component is constrained to flow normal to the openings by the application of the conditions used in determining H at these grid points. The solid

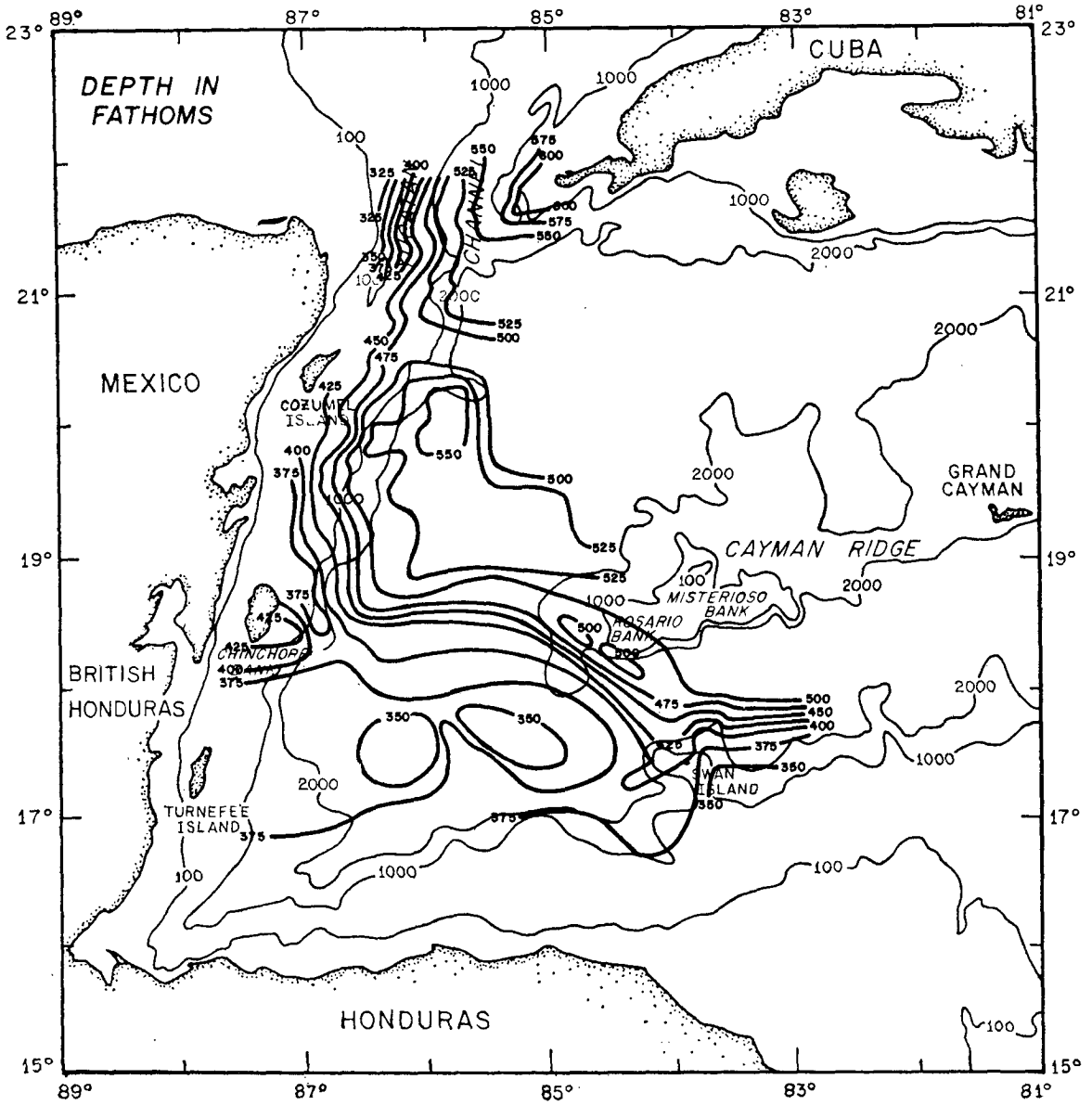

FIG. 8. The distribution of the depth, in meters, of the 11°C isotherm for July 1971.

boundary constraints are

$$B(i,2)=B(2,j)=B(5,11)=B(6,11)=0,$$
$$B(i,1)=B(i,3),$$
$$B(1,j)=B(3,j),$$
$$B(i,12)=B(i,10).$$

c. Numerical procedure

The following procedure of Wert and Reid can be applied to the numerical equations to obtain interior values of H and B, if H and α are specified at the eastern forcing boundary. At the initial time step the upper layer flow is assumed to be irrotational and geostrophic, and the lower layer at rest. The relaxation of $\nabla^2 H$ provides the upper layer thickness at $t=0$, and and a one-step Euler forward time integration of the equations gives the H field at the second time step.

The numerical analogue to (8) is then solved by a Gauss-Siedel over-relaxation scheme (Smith, 1965) to obtain successive values of H. The lower layer is kept at rest during these iterations by specifying $B=0$. The effects of initial transients are reduced by this technique (Wert and Reid, 1972).

The baroclinic calculations were continued until the changes in upper layer thicknesses were no longer significant. At that time the barotropic flow was initiated with the introduction of the numerical analogue to (9). The same procedure used to obtain upper layer thickness was followed successively to solve (8) for values of B.

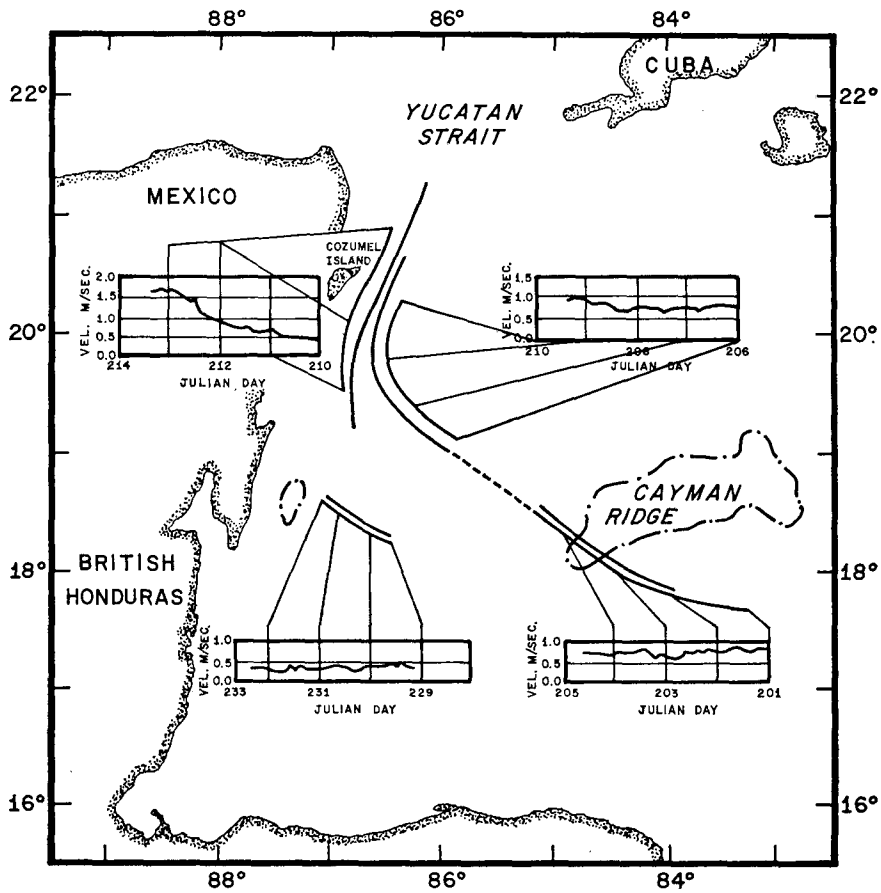

FIG. 9. Approximate drifting buoy tracklines obtained in July and August 1971. Also given are the velocities of the surface drifters.

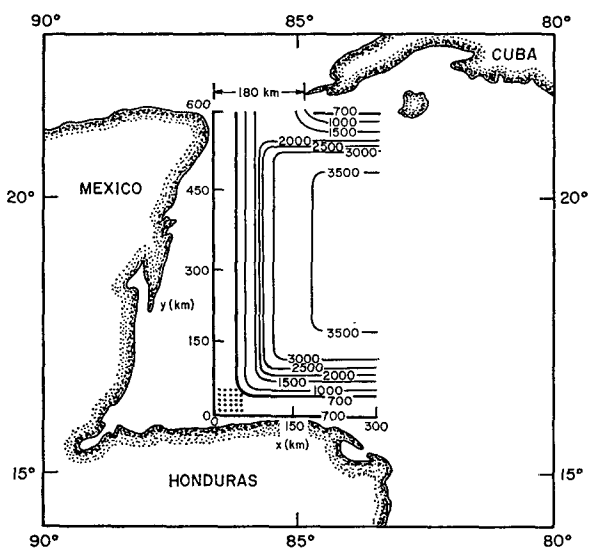

FIG. 10. The numerical model basin and its associated bottom topography, depth in meters, superimposed on a chart of the Cayman Sea. A portion of the numerical grid, with a 10 km spatial interval, is given in the lower left-hand corner of the model basin.

4. Application of the numerical model

The results of several applications of the numerical model are presented. Two of the numerical integrations consider only flow in the upper layer, while a third case allows flow in both layers. A complete parametric study involving the frictional coefficients was not conducted. However, one test was made to assess the effect of lateral friction on a steady flow regime. The results of this model are presented in the following discussion.

a. Comparison of frictional and frictionless model results

Fig. 12 gives the upper layer thicknesses determined from the frictionless inertial model of Saylor (dashed lines) and the present inertial frictional model (solid lines). In both cases the depth of the 10°C isotherm along 84°30′W during March 1958 was used to specify the geostrophic mass influx at the eastern boundary. Also, the flow is normal to the eastern boundary in both incidents.

The inertial-frictional model was spun up to nearly steady state in 600 time steps ($\Delta t = 2$ h) using a lateral frictional coefficient of 500 $m^2\ s^{-1}$. The lower layer was

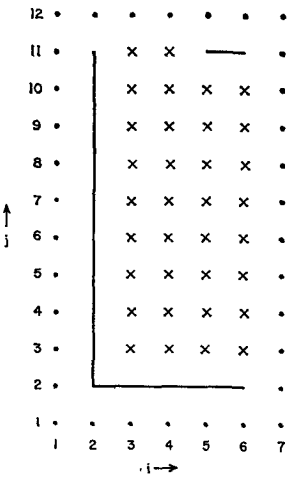

FIG. 11. A reduced version of the numerical grid used in the explanation of the boundary conditions.

kept at rest in this test. It should be noted that in the inertial model H can vary along the western solid boundary, but is a constant in the frictional case.

Viscous spreading of the boundary current at lower latitudes is evident in Fig. 12. This feature is characteristic of inertial-friction models [as noted first by Munk (1950)] in which the effect of friction is to retard the formation of the boundary current. Also, the inertial-frictional boundary current is less intense and has a more easterly core location than the purely inertial current.

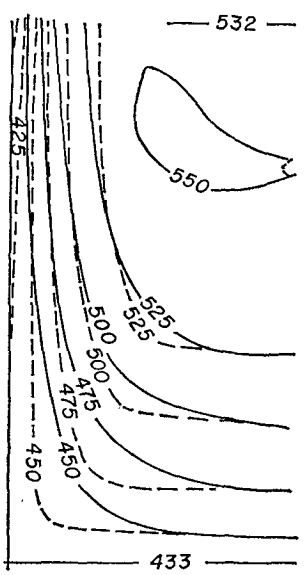

FIG. 12. Steady-state results from the present inertial-frictional model (solid lines) after a 1200 h numerical integration and the rictionless-inertial model of Saylor (dashed lines).

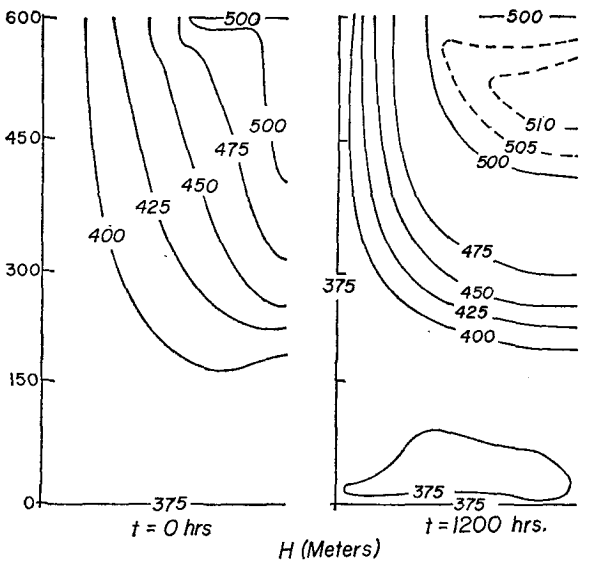

FIG. 13. The upper layer height (H), in meters, for the case of normal flow at the eastern input boundary, at $t=0$ h (left panel), and $t=1200$ h (right panel).

b. Baroclinic flow regime specifying normal flow at the eastern boundary

The mass influx required to drive the normal flow model is taken as a smoothed version of the equivalent baroclinic transport curve at 84W obtained during April–May 1968 (Fig. 5a). As the data along 84W do not extend to the Cuban coast, the values of the EBH at the western tip of Cuba are used to complete this section. The Laplacian flow pattern obtained from this influx is given in the left panel of Fig. 13. The only intensification in the flow is at the Yucatan Strait, where this constriction causes increased outward velocities at both sides.

Using the Laplacian field of Fig. 13 as the initial field of flow, the model was allowed to run for 1200 h (600 iterations) while the lower layer remained at rest. The time step and frictional coefficient were identical to the previous example. The 600th iteration (1200 h) upper layer height field is given in the right panel of Fig. 13.

The baroclinic spin-up process was essentially complete after 600 h with small, non-systematic changes occurring throughout the next 600 h. The convergence of the H lines as they approach the Yucatan Channel represents the western boundary intensification process. The maximum velocity of the flow has increased from 0.6 m s^{-1} at the eastern boundary to 0.8 m s^{-1} at the Yucatan Strait. Fig. 14 shows a plot of the north component of velocity at various latitudes, and indicates that the major accelerations have occurred by 450 km.

Fig. 15 gives the relative vorticity at two latitudes, and at the eastern opening. The maximum relative vorticity at the eastern opening is approximately one-

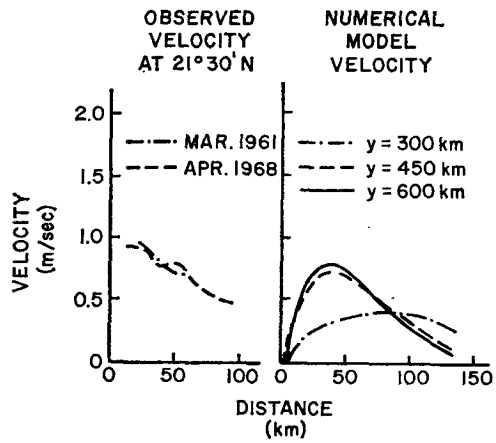

FIG. 14. Cross-stream geostrophic velocity profiles at the Yucatan Strait determined from observation (left panel) and numerical model (right panel).

quarter of the mean planetary vorticity. However, as the flow turns north and accelerates along the western boundary the cyclonic vorticity increases dramatically.

As the northward flowing current accelerates, the area under the relative vorticity curve increases. Cyclonic vorticity is being diffused into the current as a result of frictional boundary effects. Thus, the cyclonic vorticity flank of the boundary current can be considered to represent the frictional boundary layer. At the Yucatan Strait, the frictional boundary layer is only 30 km wide.

The intense northerly flow which was present at the western tip of Cuba in the Laplacian field at $t=0$ has vanished, and been replaced by a countercurrent. The southerly flow appears in response to the eastward flow at the forcing boundary. In the extreme southern basin, a closed cyclonic gyre has developed.

c. *Barotropic flow regime specifying normal flow at the eastern boundary*

At the 600th iteration, two barotropic models were initiated, one with bottom topography in the lower layer and one without. In both cases the interlayer stress coefficient σ was taken as 1×10^{-3} cm s^{-1} and the bottom stress coefficient σ' as 50×10^{-3} cm s^{-1}. The barotropic flow components of both models at 1800 and 2400 h are given in Fig. 16. Although neither model attained a steady state, it was necessary to limit both time integrations to 600 additional 2 h steps.

The effect of topography on the barotropic regime is to confine and intensify the flow along the isobaths. While the core of the non-topographic barotropic current coincides with the core of the forcing upper layer flow, the core of the topographic current is along the continental slope. Because of the shallow sill depth at the Yucatan Channel, much of the barotropic regime is forced to the east instead of flowing out of the basin to the north.

During these 1200 h, the changes occurring in the upper layer thicknesses of both the cases are small. The more intense and systematic changes occur in the topographic model along the core of the barotropic flow. However, the maximum changes are of the order of meters, which do not significantly affect the velocity distributions.

d. *Baroclinic flow regime specifying non-normal flow at the eastern boundary*

To determine the effect of varying the boundary conditions the numerical model was rerun with the model inflow angles approximating the inflow angles observed during April–May 1968. Fig. 17 gives the upper layer height field at $t=500$ h (left panel) and at $t=1000$ h (right panel). No significant upper layer height changes occurred after 1000 h.

At $t=500$ h the numerical field closely approximates the observed field as given in Fig. 4. As the time integration continues the circulation about the closed eddy in the interior of the basin becomes less intense.

5. Discussion

The dynamical processes active in the basin can be inferred from a comparison of the numerical and observational circulation regimes. For instance, the baroclinic western intensification of the model and observed flows appears similar. The largest acceleration occurs close to the Yucatan Strait in both cases, an

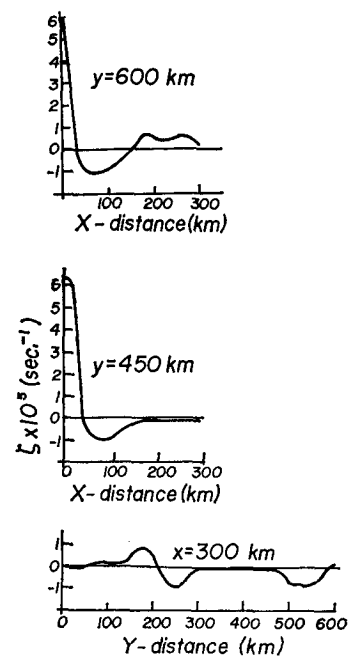

FIG. 15. The upper layer relative vorticity at $t=1200$ h, for the upper panel, latitude $y=600$ km (Yucatan Strait); middle panel, latitude $y=450$ km; and lower panel, longitude $x=300$ km (eastern input boundary).

observational feature previously noted by Cochrane (1971). The model baroclinic velocity profile at the Strait approximates the observed profile both in the speed and position of the current axis (Fig. 14).

This similarity of velocity profiles suggests that the frictional boundary layer in the actual basin is also very narrow. The observed velocity curves of Fig. 14 indicate that the cyclonic flank of the current is very close to the coastline. Molinari and Starr (1972) indicate that the relative speeds of their surface drifters (Fig. 9) in the vicinity of the Strait also suggest a narrow cyclonic boundary layer.

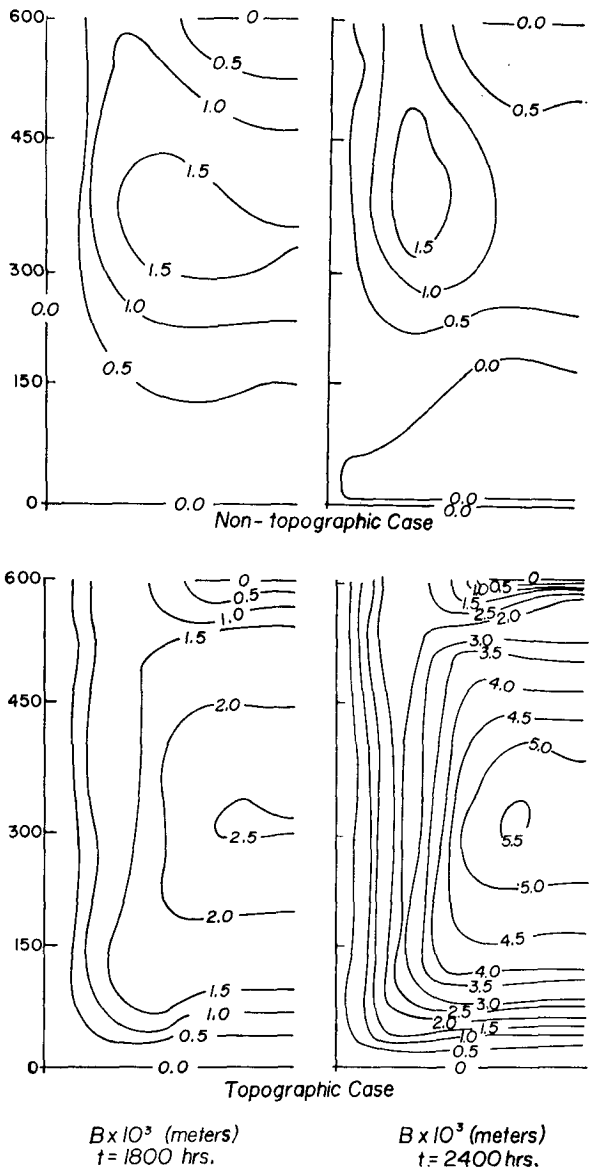

FIG. 16. The barotropic height (B), in meters, for the topographic case (lower panels) and non-topographic case (upper panels), at the time steps $t=1800$ h (left panels), and $t=2400$ h (right panels).

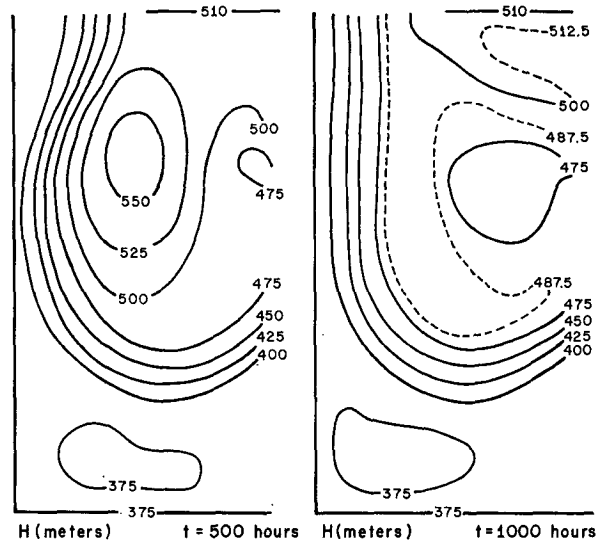

FIG. 17. The upper layer height (H), in meters, for the case of non-normal flow at the eastern input boundary, at $t=500$ h (left panel), and $t=1000$ h (right panel).

The upper layer changes noted after the initiation of the lower layer motion do not significantly affect the western boundary current, suggesting that topography is not an important factor in the baroclinic intensification. The beta-effect and advection as indicated in the Charney-Morgan inertial theories are sufficient to account for the baroclinic accelerations.

In contrast, the model barotropic component is very dependent on topographic influences. Once initiated, barotropic intensification does not occur in the vicinity of the Strait but rather along the continental slopes of the boundaries. This suggests that topography rather than the beta-effect is the prime mechanism responsible for the barotropic boundary current. The observed topographic trapping of the current (Cochrane, 1966; Molinari and Cochrane, 1972) and the model trapping of the barotropic mode of the flow suggest that, particularly at shallow depths, the barotropic component can contribute significantly to the current. However, the magnitude of this barotropic component is sensitive to changes of σ or σ'.

The influence of Cuba on the intensification process can be obtained from consideration of the flow through the Strait. Both the model and the observed data have countercurrents present at the western tip of Cuba. This separation of the main northerly flow and the island suggests that the western intensification of the Yucatan Current is dynamically independent of Cuba.

Wert and Reid varied the input at the Yucatan Strait seasonally to obtain a one-year prediction of the circulation in the Gulf of Mexico. The lack of sufficient data to realistically specify an annual variation of mass influx at 84W precludes the possibility of conducting a similar study for the Cayman Sea at the present time.

An indication of the variations occurring in the Cayman Sea circulation can be discerned from the data analysis. The July–August circulation is characterized by a more northerly development of the boundary current than occurs in the spring. This can result in a cyclonic flow pattern in the southern basin in July (Fig. 8).

The differences in the flow patterns appear to be a function of the northern component of the flow as it crosses the western Cayman Ridge. As mentioned previously the summer pattern exhibits a more northerly flow at 85W than is found in the spring. Since the angle of the flow across the Ridge is determined by conditions upstream, the cause of the variability cannot be ascertained from the data considered in this paper.

However, the data presented are consistent with other studies of the variability of the circulation pattern in this region. Perlroth (1968) conducted a compilation of bathythermographs taken in the Caribbean Sea in which he catalogued the records for two 2-month seasons. His winter results indicate less of a northerly component at 85W than do his summer results.

Acknowledgments. The contributions to this study by R. O. Reid are gratefully acknowledged. The author also wishes to express his appreciation to Mr. J. D. Cochrane for the use of his data, and to Dr. D. Fahlquist for permitting the collection of XBT data on his August 1970 cruise. This work was supported by the National Science Foundation under Grant GA-20569 to the Texas A & M University Research Foundation, and under International Decade of Ocean Exploration Grant AG-253.

REFERENCES

Ahrens, J., 1965: Potential vorticity in the thermocline of the Yucatan Current. Masters thesis, Texas A&M University, 44 pp.

Arakawa, J., 1966: Computational design of a long-term numerical integration of the equations of fluid motion: Two-dimensional incompressible flow—Part 1. *J. Comput. Phys.*, **1**, 119–143.

Cochran, J. D., 1966: The Yucatan Current. Rept., Dept. of Oceanography, Texas A&M University, Ref. 66-23-T, 14–25.

——, 1969. The currents and water masses of the eastern Gulf of Mexico and western Caribbean. Rept., Dept. of Oceanography, Texas A&M University, Ref. 69-0-T, 29–31.

——, 1971: Current observations in Yucatan Strait. *Trans. Amer. Geophys. Union*, **52**, 254 (Abstract).

Fofonoff, N., 1962: Dynamics of ocean currents. *The Sea*, Vol. 1, Interscience, 323–396.

Molinari, R. L., and J. D. Cochrane 1972: The effect of topography on the Yucatan Current. *Contributions Phys. Oceanogr. Gulf of Mexico*, Texas A&M University Oceanog. Studies, Vol. 2, L. R. A. Capurro and J. L. Reid, Eds., Gulf Publ. Co., 149–155.

——, and R. B. Starr, 1972: Lagrangian current and hydrographic measurements in the Western Caribbean Sea. *Trans. Amer. Geophys. Union*, **53**, 392 (Abstract).

Munk, W. H., 1950: On the wind-driven ocean circulation. *J. Meteor.*, **1**, 79–93.

Perlroth, I., 1968: Distribution of mass in the near surface waters of the Caribbean. Natl. Oceanog. Data Center, Progress Report No. P-72, 15 pp.

Saylor, J. H., 1963: Inertial currents in the Caribbean Sea. Masters thesis, Texas A&M University, 48 pp.

Smith, G. D., 1965: *Numerical Solution of Partial Differential Equations*. Oxford University Press, 179 pp.

Wert, R. T., and R. O. Reid, 1972: A baroclinic prognostic numerical circulation model. *Contributions Phys. Oceanogr. Gulf of Mexico*, Texas A&M Univ. Oceanogr. Studies, Vol. 2, L. R. A. Capurro and J. L. Reid, Eds., Gulf Publ. Co., 177–209.